Research Article | Vol. 8, No. 9 | 1 Sep 2018 | OPTICAL MATERIALS EXPRESS 2803
Optical Materials EXPRESS

Inkjet-printing of graphene saturable absorbers for ~2 μm bulk and waveguide lasers

PAVEL LOIKO,[1] JOSEP MARIA SERRES,[2] SZYMON SOLLAMI DELEKTA,[3] ESROM KIFLE,[2] JAKUB BOGUSŁAWSKI,[4,5] MACIEJ KOWALCZYK,[4] JAROSŁAW SOTOR,[4] MAGDALENA AGUILÓ,[2] FRANCESC DÍAZ,[2] UWE GRIEBNER,[6] VALENTIN PETROV,[6] SERGEI POPOV,[3] JIANTONG LI,[3,7] XAVIER MATEOS,[2,*] AND MIKAEL ÖSTLING[3]

[1]*ITMO University, Kronverkskiy Pr., 49, 197101 Saint-Petersburg, Russia*
[2]*Física i Cristal·lografia de Materials i Nanomaterials (FiCMA-FiCNA)-EMaS, Dept. Química Física i Inòrganica, Universitat Rovira i Virgili (URV), Campus Sescelades, E-43007 Tarragona, Spain*
[3]*School of Information and Communication Technology, KTH Royal Institute of Technology, Electrum 229, SE-164 40 Kista, Sweden*
[4]*Laser & Fiber Electronics Group, Faculty of Electronics, Wrocław University of Science and Technology, Wybrzeże S. Wyspiańskiego 27, 50-370 Wrocław, Poland*
[5]*Institute of Physical Chemistry, Polish Academy of Sciences, Kasprzaka 44-52, 01-224 Warsaw, Poland*
[6]*Max Born Institute for Nonlinear Optics and Short Pulse Spectroscopy, Max-Born-Str. 2a, D-12489 Berlin, Germany*
[7]*jiantong@kth.se*
**xavier.mateos@urv.cat*

Abstract: A technique for inkjet-printing of graphene saturable absorbers (SAs) for ~2-μm bulk and waveguide lasers is presented. Based on distillation-assisted solvent exchange to fabricate high-concentration graphene inks, this technique is capable of producing few-layer graphene films of arbitrary shape. Absorption saturation of graphene printed on glass is demonstrated at ~1.56 μm for picosecond and femtosecond pulses indicating a large fraction of the saturable losses. Inkjet-printed transmission-type graphene SAs are applied in passively Q-switched nanosecond thulium (Tm) microchip and planar waveguide lasers. The Tm microchip laser generates 136 ns / 1.2 μJ pulses at 1917 nm with a repetition rate of 0.37 MHz with a Q-switching conversion efficiency reaching 65%. The planar waveguide laser generates 98 ns / 21 nJ pulses at 1834 nm at a repetition rate in the MHz-range. The inkjet-printing technique is promising for production of patterned SAs for waveguide lasers.

OCIS codes: (160.4330) Nonlinear optical materials; (140.3540) Lasers, Q-switched; (140.3070) Infrared and far-infrared lasers; (230.7390) Waveguides, planar.

References and links

1. A. K. Geim and K. S. Novoselov, "The rise of graphene," Nat. Mater. **6**(3), 183–191 (2007).
2. Q. Bao, H. Zhang, Y. Wang, Z. Ni, Y. Yan, Z. X. Shen, K. P. Loh, and D. Y. Tang, "Atomic-layer graphene as a saturable absorber for ultrafast pulsed lasers," Adv. Funct. Mater. **19**(19), 3077–3083 (2009).
3. Q. Bao, H. Zhang, Z. Ni, Y. Wang, L. Polavarapu, Z. Shen, Q. H. Xu, D. Y. Tang, and K. P. Loh, "Monolayer graphene as saturable absorber in mode-locked laser," Nano Res. **4**(3), 297–307 (2011).
4. R. R. Nair, P. Blake, A. N. Grigorenko, K. S. Novoselov, T. J. Booth, T. Stauber, N. M. Peres, and A. K. Geim, "Fine structure constant defines visual transparency of graphene," Science **320**(5881), 1308 (2008).
5. G. Xing, H. Guo, X. Zhang, T. C. Sum, and C. H. A. Huan, "The Physics of ultrafast saturable absorption in graphene," Opt. Express **18**(5), 4564–4573 (2010).
6. F. Zhang, S. Han, Y. Liu, Z. Wang, and X. Xu, "Dependence of the saturable absorption of graphene upon excitation photon energy," Appl. Phys. Lett. **106**(9), 091102 (2015).
7. A. A. Balandin, S. Ghosh, W. Bao, I. Calizo, D. Teweldebrhan, F. Miao, and C. N. Lau, "Superior thermal conductivity of single-layer graphene," Nano Lett. **8**(3), 902–907 (2008).

#334613 https://doi.org/10.1364/OME.8.002803
Journal © 2018 Received 7 Jun 2018; revised 22 Jul 2018; accepted 23 Jul 2018; published 22 Aug 2018

Optical Materials EXPRESS

8. G. Sobon, J. Sotor, I. Pasternak, A. Krajewska, W. Strupinski, and K. M. Abramski, "Multilayer graphene-based saturable absorbers with scalable modulation depth for mode-locked Er- and Tm-doped fiber lasers," Opt. Mater. Express **5**(12), 2884–2894 (2015).
9. Q. Wang, H. Teng, Y. Zou, Z. Zhang, D. Li, R. Wang, C. Gao, J. Lin, L. Guo, and Z. Wei, "Graphene on SiC as a Q-switcher for a 2 μm laser," Opt. Lett. **37**(3), 395–397 (2012).
10. J. M. Serres, P. Loiko, X. Mateos, K. Yumashev, U. Griebner, V. Petrov, M. Aguiló, and F. Díaz, "Tm:KLu$(WO_4)_2$ microchip laser Q-switched by a graphene-based saturable absorber," Opt. Express **23**(11), 14108–14113 (2015).
11. A. Choudhary, S. J. Beecher, S. Dhingra, B. D'Urso, T. L. Parsonage, J. A. Grant-Jacob, P. Hua, J. I. Mackenzie, R. W. Eason, and D. P. Shepherd, "456-mW graphene Q-switched Yb:yttria waveguide laser by evanescent-field interaction," Opt. Lett. **40**(9), 1912–1915 (2015).
12. J. Ma, G. Q. Xie, P. Lv, W. L. Gao, P. Yuan, L. J. Qian, H. H. Yu, H. J. Zhang, J. Y. Wang, and D. Y. Tang, "Graphene mode-locked femtosecond laser at 2 μm wavelength," Opt. Lett. **37**(11), 2085–2087 (2012).
13. E. Ugolotti, A. Schmidt, V. Petrov, J. W. Kim, D.-I. Yeom, F. Rotermund, S. Bae, B. H. Hong, A. Agnesi, C. Fiebig, G. Erbert, X. Mateos, M. Aguilo, F. Diaz, and U. Griebner, "Graphene mode-locked femtosecond Yb:KLuW laser," Appl. Phys. Lett. **101**(16), 161112 (2012).
14. W. B. Cho, J. W. Kim, H. W. Lee, S. Bae, B. H. Hong, S. Y. Choi, I. H. Baek, K. Kim, D.-I. Yeom, and F. Rotermund, "High-quality, large-area monolayer graphene for efficient bulk laser mode-locking near 1.25 μm," Opt. Lett. **36**(20), 4089–4091 (2011).
15. Y. Wang, W. Chen, M. Mero, L. Zhang, H. Lin, Z. Lin, G. Zhang, F. Rotermund, Y. J. Cho, P. Loiko, X. Mateos, U. Griebner, and V. Petrov, "Sub-100 fs Tm:$MgWO_4$ laser at 2017 nm mode locked by a graphene saturable absorber," Opt. Lett. **42**(16), 3076–3079 (2017).
16. R. Lan, P. Loiko, X. Mateos, Y. Wang, J. Li, Y. Pan, S. Y. Choi, M. H. Kim, F. Rotermund, A. Yasukevich, K. Yumashev, U. Griebner, and V. Petrov, "Passive Q-switching of microchip lasers based on Ho:YAG ceramics," Appl. Opt. **55**(18), 4877–4887 (2016).
17. X. Mateos, P. Loiko, S. Y. Choi, F. Rotermund, M. Aguiló, F. Díaz, U. Griebner, and V. Petrov, "Single-walled carbon nanotubes oust graphene and semiconductor saturable absorbers in Q-switched solid-state lasers at 2 μm," Laser Phys. Lett. **14**(9), 095801 (2017).
18. H. Yu, V. Petrov, U. Griebner, D. Parisi, S. Veronesi, and M. Tonelli, "Compact passively Q-switched diode-pumped Tm:$LiLuF_4$ laser with 1.26 mJ output energy," Opt. Lett. **37**(13), 2544–2546 (2012).
19. E. Kifle, X. Mateos, P. Loiko, V. Petrov, U. Griebner, M. Aguiló, and F. Díaz, "Graphene Q-switched Tm:$KY(WO_4)_2$ waveguide laser," Laser Phys. **27**(4), 045801 (2017).
20. A. C. Ferrari, F. Bonaccorso, V. Fal'ko, K. S. Novoselov, S. Roche, P. Bøggild, S. Borini, F. H. L. Koppens, V. Palermo, N. Pugno, J. A. Garrido, R. Sordan, A. Bianco, L. Ballerini, M. Prato, E. Lidorikis, J. Kivioja, C. Marinelli, T. Ryhänen, A. Morpurgo, J. N. Coleman, V. Nicolosi, L. Colombo, A. Fert, M. Garcia-Hernandez, A. Bachtold, G. F. Schneider, F. Guinea, C. Dekker, M. Barbone, Z. Sun, C. Galiotis, A. N. Grigorenko, G. Konstantatos, A. Kis, M. Katsnelson, L. Vandersypen, A. Loiseau, V. Morandi, D. Neumaier, E. Treossi, V. Pellegrini, M. Polini, A. Tredicucci, G. M. Williams, B. H. Hong, J.-H. Ahn, J. M. Kim, H. Zirath, B. J. van Wees, H. van der Zant, L. Occhipinti, A. Di Matteo, I. A. Kinloch, T. Seyller, E. Quesnel, X. Feng, K. Teo, N. Rupesinghe, P. Hakonen, S. R. T. Neil, Q. Tannock, T. Löfwander, and J. Kinaret, "Science and technology roadmap for graphene, related two-dimensional crystals, and hybrid systems," Nanoscale **7**(11), 4598–4810 (2015).
21. F. Bonaccorso, Z. Sun, T. Hasan, and A. C. Ferrari, "Graphene photonics and optoelectronics," Nat. Photonics **4**(9), 611–622 (2010).
22. L. Zhang, H. Liu, Y. Zhao, X. Sun, Y. Wen, Y. Guo, X. Gao, C. A. Di, G. Yu, and Y. Liu, "Inkjet printing high-resolution, large-area graphene patterns by coffee-ring lithography," Adv. Mater. **24**(3), 436–440 (2012).
23. J. Li, F. Ye, S. Vaziri, M. Muhammed, M. C. Lemme, and M. Östling, "Efficient inkjet printing of graphene," Adv. Mater. **25**(29), 3985–3992 (2013).
24. F. Torrisi, T. Hasan, W. Wu, Z. Sun, A. Lombardo, T. S. Kulmala, G.-W. Hsieh, S. Jung, F. Bonaccorso, P. J. Paul, D. Chu, and A. C. Ferrari, "Inkjet-printed graphene electronics," ACS Nano **6**(4), 2992–3006 (2012).
25. G. Hu, T. Albrow-Owen, X. Jin, A. Ali, Y. Hu, R. C. T. Howe, K. Shehzad, Z. Yang, X. Zhu, R. I. Woodward, T.-C. Wu, H. Jussila, J.-B. Wu, P. Peng, P.-H. Tan, Z. Sun, E. J. R. Kelleher, M. Zhang, Y. Xu, and T. Hasan, "Black phosphorus ink formulation for inkjet printing of optoelectronics and photonics," Nature Commun. **8** (1), 278 (2017).
26. M. Singh, H. M. Haverinen, P. Dhagat, and G. E. Jabbour, "Inkjet printing-process and its applications," Adv. Mater. **22**(6), 673–685 (2010).
27. E. B. Secor, P. L. Prabhumirashi, K. Puntambekar, M. L. Geier, and M. C. Hersam, "Inkjet printing of high conductivity, flexible graphene patterns," J. Phys. Chem. Lett. **4**(8), 1347–1351 (2013).
28. L. Huang, Y. Huang, J. Liang, X. Wan, and Y. Chen, "Graphene-based conducting inks for direct inkjet printing of flexible conductive patterns and their applications in electric circuits and chemical sensors," Nano Res. **4**(7), 675–684 (2011).
29. S. Sollami Delekta, A. D. Smith, J. Li, and M. Östling, "Inkjet printed highly transparent and flexible graphene micro-supercapacitors," Nanoscale **9**(21), 6998–7005 (2017).

Optical Materials EXPRESS

30. A. C. Ferrari, J. C. Meyer, V. Scardaci, C. Casiraghi, M. Lazzeri, F. Mauri, S. Piscanec, D. Jiang, K. S. Novoselov, S. Roth, and A. K. Geim, "Raman spectrum of graphene and graphene layers," Phys. Rev. Lett. **97**(18), 187401 (2006).
31. L. M. Malard, M. A. A. Pimenta, G. Dresselhaus, and M. S. Dresselhaus, "Raman spectroscopy in graphene," Phys. Rep. **473**(5), 51–87 (2009).
32. J. Ma, G. Xie, P. Lv, W. Gao, P. Yuan, L. Qian, U. Griebner, V. Petrov, H. Yu, H. Zhang, and J. Wang, "Wavelength-versatile graphene-gold film saturable absorber mirror for ultra-broadband mode-locking of bulk lasers," Sci. Rep. **4**, 5016 (2014).
33. R. Grange, M. Haiml, R. Paschotta, G. J. Spühler, L. Krainer, M. Golling, O. Ostinelli, and U. Keller, "New regime of inverse saturable absorption for self-stabilizing passively mode-locked lasers," Appl. Phys. B **80**(2), 151–158 (2005).
34. L. Orsila, A. Härkönen, J. Hyyti, M. Guina, and G. Steinmeyer, "Ultrahigh precision nonlinear reflectivity measurement system for saturable absorber mirrors with self-referenced fluence characterization," Opt. Lett. **39**(15), 4384–4387 (2014).
35. J. M. Serres, P. Loiko, X. Mateos, H. Yu, H. Zhang, Y. Chen, V. Petrov, U. Griebner, K. Yumashev, M. Aguiló, and F. Díaz, "MoS_2 saturable absorber for passive Q-switching of Yb and Tm microchip lasers," Opt. Mater. Express **6**(10), 3262–3273 (2016).
36. V. Petrov, M. C. Pujol, X. Mateos, Ò. Silvestre, S. Rivier, M. Aguiló, R. M. Solé, J. H. Liu, U. Griebner, and F. Díaz, "Growth and properties of $KLu(WO_4)_2$, and novel ytterbium and thulium lasers based on this monoclinic crystalline host," Laser Photonics Rev. **1**(2), 179–212 (2007).
37. A. E. Troshin, V. E. Kisel, A. S. Yasukevich, N. V. Kuleshov, A. A. Pavlyuk, E. B. Dunina, and A. A. Kornienko, "Spectroscopy and laser properties of Tm:$KY(WO_4)_2$ crystal," Appl. Phys. B **86**(2), 287–292 (2007).
38. J. M. Serres, X. Mateos, P. Loiko, K. Yumashev, N. Kuleshov, V. Petrov, U. Griebner, M. Aguiló, and F. Díaz, "Diode-pumped microchip Tm:$KLu(WO_4)_2$ laser with more than 3 W of output power," Opt. Lett. **39**(14), 4247–4250 (2014).
39. M. Segura, M. Kadankov, X. Mateos, M. C. Pujol, J. J. Carvajal, M. Aguiló, F. Díaz, U. Griebner, and V. Petrov, "Passive Q-switching of the diode pumped Tm^{3+}:$KLu(WO_4)_2$ laser near 2-μm with Cr^{2+}:ZnS saturable absorbers," Opt. Express **20**(4), 3394–3400 (2012).
40. E. Kifle, X. Mateos, P. Loiko, S. Y. Choi, J. E. Bae, F. Rotermund, M. Aguiló, F. Díaz, U. Griebner, and V. Petrov, "Tm:KY_1-x-yGdxLuy$(WO_4)_2$ planar waveguide laser passively Q-switched by single-walled carbon nanotubes," Opt. Express **26**(4), 4961–4966 (2018).
41. A. S. Yasukevich, P. Loiko, N. V. Gusakova, J. M. Serres, X. Mateos, K. V. Yumashev, N. V. Kuleshov, V. Petrov, U. Griebner, M. Aguiló, and F. Díaz, "Modeling of graphene Q-switched Tm lasers," Opt. Commun. **389**, 15–22 (2017).

1. Introduction

Graphene is a two-dimensional layer of carbon atoms arranged in a honeycomb lattice [1]. In recent years, it has been recognized as an attractive material for saturable absorbers (SAs) employed to passively modulate the losses in near-IR lasers [2,3]. Graphene has a unique zero-bandgap feature with the hollow cone electron and hole bands meeting at the Dirac point. This property leads to a broadband linear (low-signal) absorption (at 0.4 – 3 μm) which is anomalously strong, about 2.3%, for a single atomic layer [4]. Graphene also exhibits broadband (at 0.8 – 2.8 μm) ultrafast saturable absorption due to the finite number of electronic states in the valence band [5,6]. It features a relatively low saturation fluence (intensity), a fast recovery of the initial absorption (with two characteristic time constants, ~200 fs and ~1 ps [2], respectively) and a reasonably low laser-induced damage threshold. The latter is related to very high thermal conductivity of graphene [7]. The modulation depth of graphene SAs can be altered by stacking several carbon layers [5,6,8]. These properties have motivated multiple studies of graphene SAs in passively Q-switched (PQS) [9–11] and mode-locked (ML) [12–15] bulk and waveguide lasers emitting in the near-IR spectral range.

The application of graphene in pulsed lasers emitting at ~2 μm is particularly attractive. Due to the graphene band structure, the absorption saturation properties of graphene are wavelength-dependent, i.e., the saturation fluence (intensity) decreases at lower photon energy [6]. The ~2 μm laser emission is eye-safe, typically achievable with thulium (Tm^{3+}, $^3F_4 \rightarrow {}^3H_6$ transition) or holmium (Ho^{3+}, $^5I_7 \rightarrow {}^5I_8$ transition) ions. Pulsed (nanosecond) ~2 μm lasers are used in range-finding, environmental sensing, wind mapping, spectroscopy and medicine. Regarding ML lasers at ~2 μm, graphene can be a competitor of the GaSb-based semiconductor SAs (SESAs) where the technology is far from being mature. Indeed, recently, a graphene SA was successfully employed in a bulk ML Tm laser generating for the first time

Optical Materials EXPRESS

sub-100 fs pulses at ~2 μm [15]. As for PQS lasers emitting at ~2 μm, graphene can be treated as a "fast" SA leading to the generation of nanosecond pulses at high repetition rates [10,16]. Similar to the case of ML lasers, it was argued that graphene SA is a competitor of the SESAs in such lasers as well [17]. Note that there also exist efficient "slow" SAs for PQS ~2 μm lasers (e.g., Cr^{2+}:ZnS(e) crystals and ceramics) which, however, operate in a different regime providing high energy pulses at low repetition rates [18]. Graphene is attractive for PQS waveguide lasers since it can be used in different geometries (transmission-type [19] or evanescent-field interaction) [11]. Such lasers are of interest in integrated optics for sensing applications.

Several methods have been proposed for the fabrication of graphene on various substrates (e.g., Si, SiC, glass, metals, etc.). Mostly investigated are the mechanical and liquid phase exfoliation of graphite or graphite oxide, epitaxial growth on SiC and metals, and chemical vapor deposition (CVD) [20]. Among these, the exfoliation methods yield graphene in the form of small-size graphene flakes which can then be deposited as thin films with tailorable optical and electrical properties [21]. In this relation, the inkjet printing technique has gained a lot of research interest as it enables the deposition of various functional materials, e.g., graphene nanostructures (graphene, graphene oxide, carbon nanotubes, etc.) [22–24] and other 2D materials (e.g., black phosphorus) [25]. This method offers simplicity, cost-efficiency, scalability and versatility provided by the direct patterning feature, allowing fabrication of functional devices and thin films through the controlled ejection of droplets of liquid phase material (ink) from the nozzle onto a substrate.

It is crucial to fine-tune certain properties of graphene inks for obtaining a precise and reliable jetting. These include relevant fluidic properties (viscosity and surface tension), acceptable concentration of graphene flakes while avoiding aggregation and restacking, low toxicity and small lateral dimensions of the graphene flakes to avoid nozzle clogging [26]. Efficient techniques for inkjet-printing of graphene have been proposed [23,27].

To date, inkjet-printed graphene and graphene oxide devices have been mostly intended for electronics applications, such as sensors, transparent conductors, supercapacitors, thin film transistors, etc [24,28,29]. We report herein on the application of an inkjet-printing technique for the size-scalable production of high-quality graphene SAs for PQS ~2 μm lasers in bulk and waveguide geometry.

2. Experimental

2.1 Inkjet-printing of graphene SA

The graphene ink was prepared through the distillation-assisted solvent exchange technique [23]. First, graphene flakes were obtained through the exfoliation by ultrasonication of graphite in dimethylformamide (DMF). Next, 8 mg/ml of ethyl cellulose (22 cP for 5 w/v% in 80:20 toluene:ethanol, Sigma-Aldrich, product no. 200697) and 2 mg/ml of ethyl cellulose (4 cP for 5 w/v% in 80:20 toluene:ethanol, Sigma-Aldrich, product no. 200646) were added to stabilize the graphene flakes and the solvent (DMF) was exchanged with terpineol through distillation. Last, the dispersion was diluted with ethanol at the volume ratio of 3:1 (terpineol: ethanol) thus obtaining the final ink with an estimated graphene concentration of ~0.5 mg/ml.

The graphene film was printed with a commercial inkjet printer (Dimatix Materials Printer, DMP 2800, Dimatix-Fujifilm Inc.) equipped with 10 pl cartridges (DMC-11610). The graphene films were fabricated with 20 printing passes, a drop spacing of 40 μm, a jetting voltage of 27 V and a plate temperature of 45 °C. The substrate was a microscope glass slide (SuperFrost Slides, VWR, product no. 631-0114, 1-1.2 mm thick). After printing, the films were dried at 80 °C for 1 h and annealed at 400 °C for 1 h.

Optical Materials EXPRESS

2.2 Material characterization

The morphology of the graphene film was studied with a Scanning Electron Microscope (SEM, Zeiss Ultra 55). The small-signal transmission spectra were measured with a Varian CARY-5000 spectrophotometer. The Raman spectra were measured with a calibrated home-made spectrometer (KTH) using an Ar^+ ion laser (514 nm) as an excitation source.

The absorption saturation of the inkjet-printed graphene SA was studied by an open-aperture Z-scan method. The sample was translated along the focused beam of a pulsed laser providing variation of the peak fluence F incident on the sample. We used a ML Er-doped fiber laser emitting at 1560 nm with a repetition rate of 100 MHz (Menlo T-Light). The pulse duration $\Delta\tau$ was adjusted with an external dispersion-managed fiber path to 65 fs or 1 ps (determined as full width at half maximum, FWHM, under Gaussian shape assumption). The Gaussian radius of the laser beam in the focus w_L was 9 μm and the Rayleigh length z_R was 0.16 mm. The peak laser fluence is $F = 2E/(\pi w_L^2)$, where E is the pulse energy. For the designed set-up, the variation of F was in the range 1...400 μJ/cm^2.

3. Characterization of the inkjet-printed graphene SA

3.1 Morphology

In Fig. 1, we show a secondary electron high-contrast SEM image. Graphene flakes with lateral dimensions of <1 μm are observed. During their deposition by inkjet printing, they are arranged with different orientations forming a thin film with an almost uniform thickness. The flakes located at the surface have a tendency of protruding, increasing the surface area of the sample. Only a small amount of ethyl cellulose residue in the form of tiny white particles can be noticed, confirming that annealing of the sample was efficient. The thickness of the graphene thin film was measured by a profilometer [29] to be around 27 nm with a roughness R_a of 3-5 nm, partially affected by inherent roughness of the glass substrate.

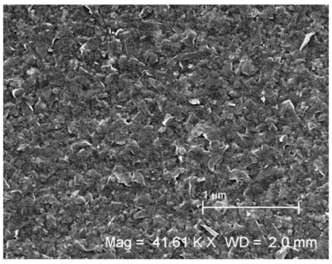

Fig. 1. Scanning Electron Microscope (SEM) image of the inkjet-printed graphene film exhibiting sharp graphene flakes.

3.2 Linear transmission

The low-signal transmission (T_0) spectrum of the film is shown in Fig. 2. The value of T_0 is determined by subtracting the Fresnel losses from the substrate, i.e. $T_0 = T$ (graphene + substrate) / T(substrate).

Optical Materials EXPRESS

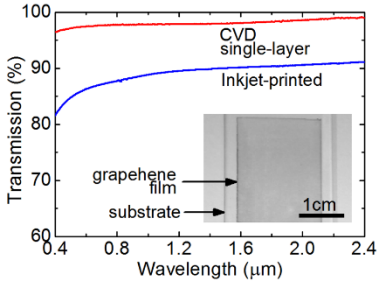

Fig. 2. Small-signal transmission, T(graphene + substrate) / T(substrate), spectrum of the inkjet-printed graphene film, *inset* – photograph of the SA; the spectrum for a CVD-grown single carbon layer graphene SA is shown for comparison [10].

The graphene film exhibits a broadband linear absorption. At ~1 μm, T_0 = 88.8% (small-signal absorption, $\alpha'_0 = 1 - T_0 = 11.2\%$). It is known that the absorption of a single carbon layer is about $\pi\alpha \approx 2.3\%$ where $\alpha \approx 1/137$ is the fine structure constant [4] and it scales linearly with the number of carbon layers n [6]. Indeed, for a commercial graphene SA containing a single carbon layer deposited by the CVD method [10], T_0 is 97.7% at ~1 μm (Fig. 2). Thus, we can estimate that the effective number of carbon layers $\langle n \rangle$ for the studied sample is between 4 and 5. Near 2 μm, T_0 for the studied sample is 90.5%.

3.3 Raman spectroscopy

The presence of the two-dimensional graphene structure was confirmed by Raman spectroscopy, see Fig. 3. The excitation wavelength was 514 nm. In Fig. 3, the spectrum of the single layer CVD-grown graphene SA is also shown for comparison (not in scale). For inkjet-printed graphene, the peak at 1582 cm^{-1} (G) exhibits a double-peak structure due to the double-degenerated (in-plane transverse optical, iTO, and longitudinal optical, LO) phonon mode E_{2g} at the Brillouin zone center. The peak at 2702 cm^{-1} (2D, also referred as G') is due to a second order process of the zone boundary phonons (two iTO phonons at the K point). The D peak with the frequency of about 1/2 of that of the 2D one (1354 cm^{-1}) arising from one iTO phonon and a defect is visible in the spectrum of the inkjet-printed graphene film. Its observation is due to the structure defects inherent to the finite size of the graphene flakes. The weak D' peak (1623 cm^{-1}) is also due to the defects. The weak and broad peak at ~2450 cm^{-1} (G*) originates from a combination of the zone boundary in-plane longitudinal acoustic, iLA, and iTO phonon modes. The interpretation of the Raman spectra is according to the previous papers [30,31].

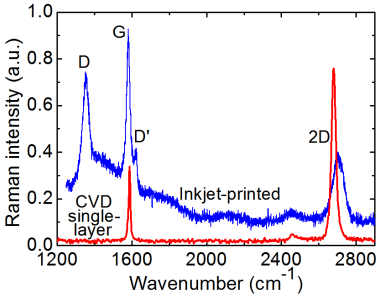

Fig. 3. Raman spectrum of the inkjet-printed graphene film, the excitation wavelength is 514 nm. The spectrum for a CVD-grown single carbon layer graphene SA is shown for comparison [10].

The increase of n (number of layers) affects strongly the Raman spectra, e.g., it modifies the spectral shape of the 2D band and the intensity ratio of the 2D and G ones [30,31]. From the broadening of the 2D band and its shift to higher frequencies, we estimate n for the inkjet-

Optical Materials EXPRESS

printed graphene film as 3-5 [30]. The corresponding ratio $I(2D)/I(G)$ is ~0.45 supporting this conclusion (compare with $I(2D)/I(G) = 2.2$ for the single carbon layer CVD-grown graphene). As a conclusion, the Raman observations are in good agreement with the absorption spectroscopy.

3.4 Absorption saturation

The open-aperture Z-scan absorption saturation curves of the inkjet-printed graphene SA are shown in Fig. 4. The intrinsic sample transmission T (i.e., after subtracting the Fresnel losses) can be represented as $T(F) = 1 - \alpha'(F)$, where α' is the sample absorption. For $F \approx 0$ (low-signal regime), $T_0 = 1 - \alpha'_0$ and $\alpha'_0 = \alpha'_S + \alpha'_{NS}$, where α'_S and α'_{NS} are the saturable and non-saturable absorption, respectively. Both pulse durations are shorter than the characteristic recovery time of initial absorption of graphene SA τ_{rec}, ~1.3 ps, as measured by the pump-probe method at ~1.5 μm [32]. Thus, the following expression can be used to model the measured absorption saturation curves [33,34]:

$$T(F) = 1 - \alpha'_{NS} - \alpha'_S \cdot \frac{1 - \exp(-F / F_{sat})}{F / F_{sat}}. \quad (1)$$

where F_{sat} is the saturation fluence which corresponds to the reduction of the saturable part of absorption by a factor of $1/e$, and the two-photon absorption (TPA) is neglected.

For the 1 ps pulses, Fig. 4(a), the best-fit parameters are $\alpha'_S = 6.5\%$ and $F_{sat} = 102$ μJ/cm^2. The corresponding saturation intensity I_{sat} is 170 MW/cm^2. Note that F_{sat} corresponds to the reduction of the saturable part of absorption by a factor of $1/e$ and I_{sat} – by a factor of ½, so there is no straightforward relation between these parameters. The ratio of the saturable to the total (low-signal) absorption α'_S/α'_0 is 0.68. For the 65 fs pulses, Fig. 4(b), $\alpha'_S = 6.8\%$ and $F_{sat} = 60$ μJ/cm^2 ($I_{sat} = 1.36$ GW/cm^2), so that $\alpha'_S/\alpha'_0 = 0.71$. For both measurements shown in Fig. 4, when the laser spot size on the sample $2w_L$ was larger than 230 μm (for $F < 20$ μJ/cm^2), the laser beam was slightly distorted due to the sample inhomogeneity. For smaller beam spot sizes, the signal was free of parasitic modulation.

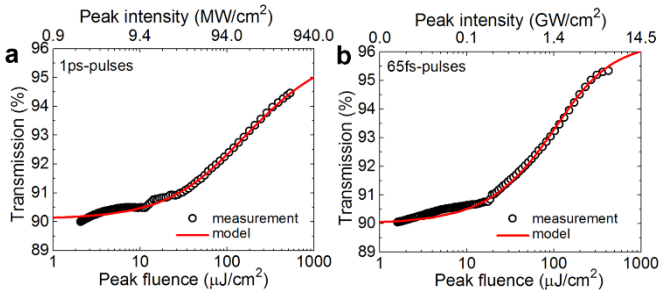

Fig. 4. (a,b) Absorption saturation curves for the inkjet-printed graphene SA measured at 1.56 μm with (a) 1 ps and (b) 65 fs pulses: *circles* – experimental data, *curves* – their fitting with Eq. (1).

For bulk solid-state lasers PQS by graphene SAs, the characteristic time of formation of a single Q-switched pulse is between few hundreds of ns to few μs [10]. This is longer than τ_{rec} of graphene, so that it is considered as a "fast" SA. It will be saturated by the instantaneous pulse intensity $I = F/\Delta\tau^*$, $\Delta\tau^* \approx 1.06\Delta\tau$ [35]. Under the "slow" SA condition (i.e., for pulse duration $\Delta\tau$ shorter than τ_{rec}) satisfied in graphene ML lasers, the absorption is saturated (bleached) by the pulse fluence.

Previously, I_{sat} for graphene SAs containing few carbon layers was measured to be about 1 MW/cm^2 for ns-long pulses and for a relatively large laser spot size of hundreds of μm [6]. A similar value was estimated from modelling the laser performance of graphene PQS lasers [16,35]. However, as it was shown in Ref [6]. for small laser spot sizes, the measured I_{sat} can

Optical Materials EXPRESS

increase by a factor of ~10 due to the effect of the carrier recombination beyond the excitation region induced by carrier diffusion. Even a further increase of I_{sat} is expected when the pulse duration $\Delta\tau$ approaches the electron-hole recombination time for graphene (~1.67 ps), so that the photo-carrier density dynamics is in a transient state [6]. Such enhancement of I_{sat} up to GW/cm^2-range due to the small laser spot size and short $\Delta\tau$ is indeed observed from our experiments.

4. Passive Q-switching of thulium lasers

The fabricated inkjet-printed graphene SA was used in two types of Tm lasers: a microchip (bulk) and a planar waveguide geometry for PQS. The transmission-type SA was inserted at a normal incidence of the mode propagation in both lasers resulting in stable passive Q-switching. As a gain material, we used Tm^{3+}-doped monoclinic double tungstates (MDTs) [36], $KRE(WO_4)_2$ (shortly KREW), where RE = Lu or Y. These crystals are known for their advantageous spectroscopic properties when doped with Tm^{3+} ions [36,37] allowing for efficient laser operation in the CW [36,38] and the PQS regime [39]. MDTs are optically biaxial, so that the optical and spectroscopic properties are described in the optical indicatrix frame with the principal axes N_p, N_m and N_g.

4.1 Laser set-ups

The scheme of the microchip (bulk) laser is shown in Fig. 5. This laser was based on a 5 at.% Tm:KLuW crystal grown by the Top-Seeded Solution Growth (TSSG) method [36]. The laser crystal was cut for light propagation along the N_g-axis enabling microchip laser operation [38]. The 4.1 mm-thick active element (aperture: $3(N_m) \times 3(N_p)$ mm^2) was polished to laser quality, wrapped with In foil and mounted in a Cu-holder water-cooled down to 12 °C.

The crystal was pumped through the pump mirror (PM) by a fiber-coupled AlGaAs laser diode (fiber core diameter: 200 µm, numerical aperture, N.A. = 0.22) emitting at ~802 nm ($^3H_6 \rightarrow {}^3H_4$ transition of Tm^{3+}). The unpolarized pump radiation was collimated and focused into the crystal by a lens assembly (1:1 reimaging ratio, 30 mm focal length). The pump spot size $2w_p$ in the crystal was 200 µm and the pump absorption under lasing conditions was 54%.

The plano-plano laser cavity comprised a flat PM, antireflection coated for 0.78–1.0 µm and high-reflection coated for 1.84–2.1 µm, and a flat output coupler (OC) with a transmission T_{OC} of 5%, 9%, 20% or 30% at the laser wavelength. The graphene SA was inserted between the active element and OC. All the optical elements in the cavity were placed next to each other in order to minimize the cavity roundtrip time and to shorten the pulses in the PQS regime. The calculated size of the laser mode on the SA was ~70 µm.

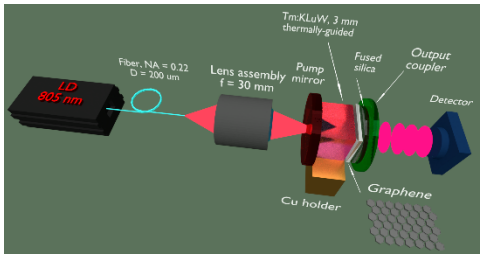

Fig. 5. Set-up of the microchip Tm laser passively Q-switched by inkjet-printed graphene SA.

The second laser studied was a planar waveguide Tm laser, see Fig. 6. It was based on a thin film with a composition of $KY_{0.61}Gd_{0.22}Lu_{0.12}Tm_{0.05}(WO_4)_2$ (abbreviated: 5 at. % Tm:KYW) grown by the Liquid Phase Epitaxy (LPE) method on an undoped (010)-oriented 2-mm thick undoped $KY(WO_4)_2$ substrate. The substrate itself was grown by the TSSG method. The top surface and both edge faces of the Tm:KYW/KYW epitaxy were polished to laser quality and remained uncoated. After polishing, the active layer thickness was 18 µm, as

Optical Materials EXPRESS

determined with ESEM measurement. The layer was oriented for light propagation along the N_g-axis with a length of 5.0 mm. The waveguide propagation losses were estimated from the Caird analysis for CW operation mode as 0.7 ± 0.2 dB/cm [40]. The epitaxy was mounted on a BK7 glass block and it was passively-cooled.

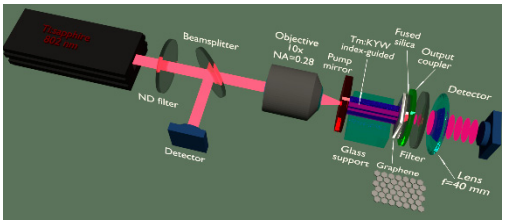

Fig. 6. Set-up of the planar waveguide Tm laser passively Q-switched by inkjet-printed graphene SA.

The active layer was pumped by a CW Ti:Sapphire laser at 802 nm. The pump polarization corresponded to $\boldsymbol{E} \parallel N_m$ in the active layer. The pump was coupled into the waveguide by a 10 × microscope objective lens (N.A. = 0.28, focal length: 20 mm) resulting in a spot diameter of 20 μm. ~48% of the incident pump power was launched into the active layer and >85% of that was absorbed under lasing conditions.

The laser cavity was composed by a flat PM and a flat OC with T_{OC} = 30% at the laser wavelength (see the details above). This OC was selected because it was difficult to achieve stable passive Q-switching for lower T_{OC}. The graphene SA was inserted between the active layer and OC minimizing the air gaps.

4.2 Microchip Tm laser

At first, we studied the CW performance of the microchip Tm laser (with SA removed from the cavity). The best output performance corresponded to T_{OC} = 9%, namely 1.38 W at 1946 nm with a slope efficiency η of 60% (with respect to the absorbed pump power P_{abs}). The laser threshold was at P_{abs} = 0.61 W. For CW experiment, we limited P_{abs} to ~3 W because Q-switching was not stable for higher pump powers. With increase of the output coupling, the emission wavelength experienced a blue-shift from 1945 to 1960 nm (for T_{OC} = 5%) to 1923 nm (for T_{OC} = 30%).

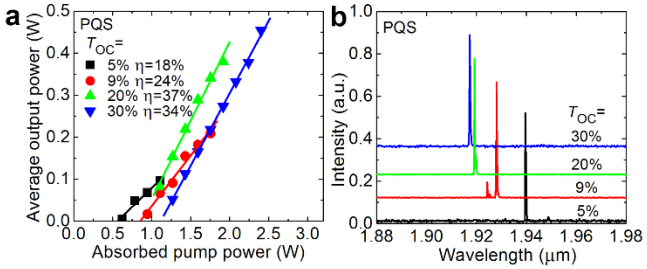

Fig. 7. (a,b) Diode-pumped Tm:KLuW microchip laser passively Q-switched by inkjet-printed graphene SA; (a) input-output dependences, η – slope efficiency (laser polarization: $\boldsymbol{E} \parallel N_m$); (b) typical laser emission spectra measured at maximum P_{abs}.

With inserted graphene SA, a stable Q-switching regime was achieved. For all output couplers (OCs), there existed an upper power limit for the Q-switching stability related to heating of the SA by the residual (non-absorbed) pump power [10]. This limit clearly increased with T_{OC}, probably due to the corresponding reduction of the intracavity peak intensity. Below this limit, no damage of the graphene SA was observed. The results in terms of output power and laser emission spectra are shown in Fig. 7. The highest average output power corresponded to the highest studied T_{OC} of 30%, namely 454 mW at 1917 nm with η =

Optical Materials EXPRESS

34%. The laser threshold was at P_{abs} = 1.12 W. The Q-switching conversion efficiency with respect to the CW mode η_{conv} was 65% indicating a moderate insertion loss of the SA. With the increase of the output coupling, a blue-shift of the emission wavelength from 1940 nm for T_{OC} = 5% to 1917 nm for T_{OC} = 30% was observed due to the quasi-three-level nature of the Tm^{3+} laser in agreement with the gain spectra of Tm:KLuW for light polarization $\boldsymbol{E} \parallel N_m$ [36]. The emission spectrum of the PQS laser typically contained one single intense line. The laser output was linearly polarized ($\boldsymbol{E} \parallel N_m$) for all OCs; the polarization was naturally selected by the anisotropy of the gain. The output beam corresponded to a TEM_{00} mode (measured M^2 parameter: <1.2).

The pulse duration $\Delta\tau$ (determined as FWHM) and the pulse repetition frequency (PRF) were measured directly, and the pulse energy was determined as $E_{out} = P_{out}/PRF$, see Fig. 8. The pulse characteristics were dependent on the absorbed pump power: $\Delta\tau$ decreased, PRF increased, and E_{out} first increased and then saturated with P_{abs}. Such a behaviour is typical for quasi-three-level lasers PQS by "fast" SAs and it is related to the dynamic bleaching of the SA [41]. For T_{OC} = 30%, the pulse duration shortened from 556 to 136 ns, and the PRF increased almost linearly from 111 to 372 kHz. The maximum pulse energy was 1.2 μJ. This corresponded to the maximum peak power $P_{peak} = E_{out}/\Delta\tau$ of 8.3 W. With increasing T_{OC}, a tendency to shorten the pulse duration and to increase the pulse energy was observed.

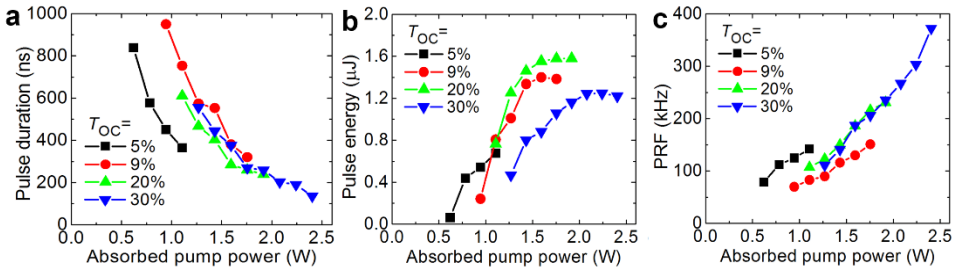

Fig. 8. (a-c) Diode-pumped Tm:KLuW microchip laser PQS by inkjet-printed graphene SA: (a) pulse duration (FWHM); (b) pulse energy; (c) pulse repetition frequency (PRF). T_{OC} is the transmission of the output coupler.

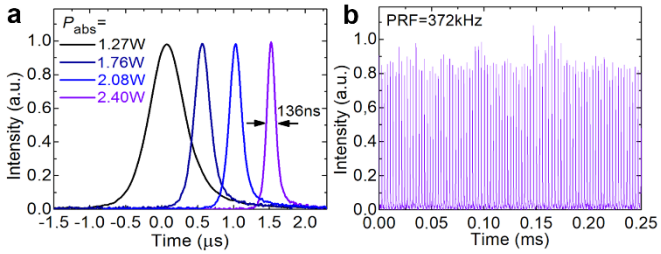

Fig. 9. Oscilloscope traces of (a) single Q-switched pulses for different absorbed pump powers P_{abs} and (b) the corresponding pulse train for P_{abs} = 2.40 W for the diode-pumped Tm:KLuW microchip laser PQS by inkjet-printed graphene SA.

The oscilloscope traces of the single Q-switched pulses obtained for T_{OC} = 30% at different absorbed pump powers are shown in Fig. 9(a). The pulses exhibit a Gaussian temporal shape. The corresponding pulse train for the maximum P_{abs} of 2.40 W is shown in Fig. 9(b). The intensity fluctuations are <20% and the room-mean-square (rms) pulse-to-pulse timing jitter is <15%. These instabilities are attributed to heating of the SA by the residual pump.

4.3 Planar waveguide Tm lasers

The input-output dependences and the typical laser emission spectra of the CW and PQS Tm:KYW planar waveguide laser are shown in Fig. 10. In the CW regime, the maximum

Optical Materials EXPRESS

output power was 132 mW at 1839.2 nm with a slope efficiency η of 52.2%. The laser threshold was at P_{abs} = 104 mW.

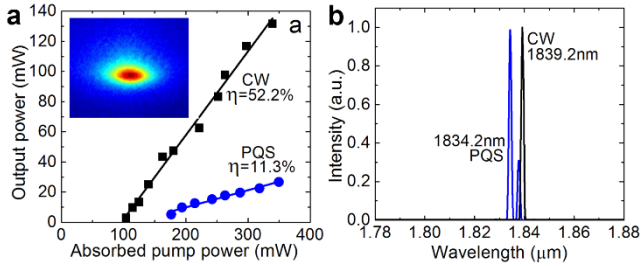

Fig. 10. (a,b) Ti:Sapphire laser pumped Tm:KYW planar waveguide laser: CW operation and PQS by the inkjet-printed graphene-SA: (a) input-output dependences, η – slope efficiency (the laser polarization is $\boldsymbol{E} \parallel N_m$), *inset* – typical spatial profile of the laser mode in the far-field (CW regime), (b) typical laser emission spectra measured at maximum P_{abs}.

With inserted graphene SA into the laser cavity, a stable Q-switching regime was observed. The maximum average output power was 26.7 mW at 1834.2 nm with η = 11.3%. The laser threshold was at P_{abs} = 170 mW and the Q-switching conversion efficiency η_{conv} was 20%. No damage of the SA was observed. A profile of the elliptic output laser beam (multimode) captured in the far-field is shown as an inset in Fig. 10(a). The laser output was linearly polarized ($\boldsymbol{E} \parallel N_m$). The shorter emission wavelength observed for the waveguide laser is due to its higher losses compared to the microchip laser and it agrees with the gain spectra of Tm:KYW [37].

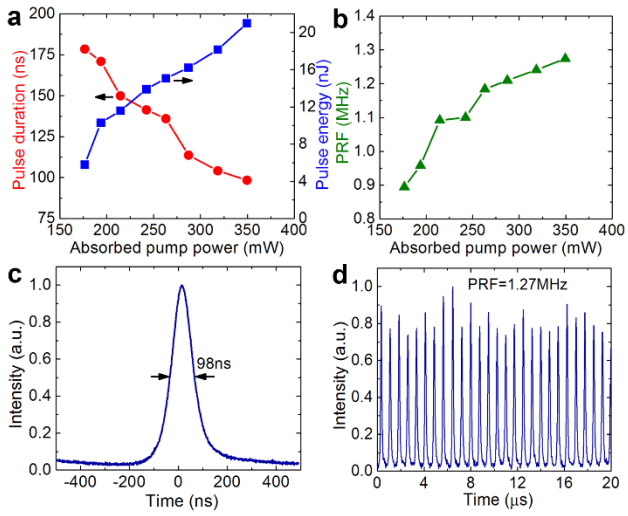

Fig. 11. (a-d) Ti:Sapphire laser pumped Tm:KYW planar waveguide laser PQS by the inkjet-printed graphene SA: (a) pulse duration (FWHM) and pulse energy; (b) pulse repetition frequency (PRF); (c,d) oscilloscope traces of (c) the shortest single Q-switched pulse and (d) the corresponding pulse train for P_{abs} = 0.35 W. T_{OC} = 30%.

The pulse characteristics of the PQS Tm:KYW planar waveguide laser are shown in Fig. 11(a,b). Similarly to the case of the microchip Tm laser, they varied with P_{abs}. The pulse duration $\Delta\tau$ decreased from 178 to 98 ns, the pulse energy E_{out} increased from 5.8 to 21 nJ, and the PRF increased almost linearly from 0.89 to 1.27 MHz. The maximum peak power P_{peak} thus reached 0.2 W. The observed higher PRFs as compared to the microchip Tm laser are due to the small size of the laser mode in the waveguide laser. The latter limits the pulse energy as expected from the theory of graphene PQS lasers [41]. The oscilloscope traces of

Optical Materials EXPRESS

the shortest single Q-switched pulse and the corresponding pulse train are shown in Fig. 11(c,d). The intensity fluctuations are <25%.

In Table 1, we compare the PQS output characteristics of the microchip and waveguide Tm lasers studied in the present work employing an inkjet-printed graphene SA with those reported recently for a commercial single carbon layer CVD-grown graphene SA [10,19]. The results obtained in the present work are superior in comparison to the previous studies. We attribute this improvement to a higher modulation depth of the inkjet-printed graphene film (Fig. 4) and, possibly, to the larger surface area of the protruded graphene flakes, Fig. 1.

Table 1. Output Characteristics of Thulium Lasers PQS by Commercial CVD-Grown and Inkjet-Printed Graphene SAs

Laser	Graphene-SA	P_{out}, mW	η, %	η_{conv}, %	E_{out}, μJ	$\Delta\tau$, ns	PRF, MHz	Ref.
Microchip	CVD	310	13	24	1.6	285	0.19	[10]
	Inkjet	454	34	65	1.2	136	0.37	*
Waveguide	CVD	6.5	9	45	0.006	195	1.13	[19]
	Inkjet	26.7	11.3	20	0.021	98	1.27	*

*This work.

5. Conclusion

We report on the successful application of inkjet-printing for the fabrication of high-quality few carbon layer graphene SA. Its nonlinear absorption characteristics were studied by the Z-scan technique at 1.5 μm using fs- and ps-long pulses resulting in a relatively high fraction of the saturable losses. The suitability of the inkjet-printed graphene SA for passive Q-switching in the ~2 μm spectral range was demonstrated using Tm^{3+}-doped microchip (bulk) and planar waveguide lasers capable of generating nanosecond pulses at high repetition rates (hundreds of kHz to MHz). The microchip (thermally guided) diode-pumped Tm:KLuW laser and the Ti:Sapphire laser pumped planar waveguide (index guided) Tm:KYW / KYW laser both passively Q-switched by the transmission-type inkjet-printed graphene SA generated 1.2 μJ / 136 ns and 98 ns / 21 nJ pulses at 0.35 MHz and 1.27 MHz repetition rates, respectively. Inkjet-printing can be applied to deposit graphene films directly on crystal faces, e.g., for passive Q-switching of ~2 μm (Tm and Ho) waveguide lasers by evanescent field interaction. Further efforts will be devoted to the application of inkjet-printed graphene SAs in mode-locked ~2 μm lasers. The inkjet-printing technique can be also applied to deposit different nanostructured absorbers, e.g. single-walled carbon nanotubes (SWCNTs) or 2D materials on dielectric substrates.

Funding

Spanish Government (MAT2016-75716-C2-1-R, (AEI/FEDER,UE) TEC 2014-55948-R); Generalitat de Catalunya (2017SGR755); National Science Centre (NCN), Poland (UMO-2015/18/E/ST7/00296).

Acknowledgments

E. K. acknowledges financial support from the Generalitat de Catalunya under grants 2016FI_B00844 and 2017FI_B100158. F. D. acknowledges additional support through the ICREA academia award 2010ICREA-02 for excellence in research. M. K. acknowledges the doctoral fellowship from the National Science Centre (NCN, Poland) under grant No. UMO-2017/24/T/ST7/00234. P. L. acknowledges financial support from the Government of the Russian Federation (grant No. 074-U01) through ITMO Post-Doctoral Fellowship scheme.